© 2017 Dhruv Gelda

REDUCING EXTRINSIC DAMPING OF SURFACE ACOUSTIC WAVES AT GIGAHERTZ FREQUENCIES

BY

DHRUV GELDA

THESIS

Submitted in partial fulfillment of the requirements
for the degree of Master of Science in Mechanical Engineering
in the Graduate College of the
University of Illinois at Urbana-Champaign, 2017

Urbana, Illinois

Adviser:

Associate Professor Sanjiv Sinha

ABSTRACT

High-frequency surface acoustic waves (SAWs) in the GHz range can be generated using absorption from an ultrafast laser in a patterned metallic grating on a substrate. Reducing the attenuation at these frequencies can yield better sensors as well as enable them to better probe phonon and electron-phonon interactions near surfaces. It is not clear from existing experiments which mechanisms dominate damping at high frequencies. We calculate damping times of SAWs due to various mechanism in the 1-100 GHz range to find that mechanical loading of the grating on the substrate dominates dissipation by radiating energy from the surface into the bulk. To overcome this and enable future measurements to probe intrinsic damping, we propose incorporating distributed acoustic Bragg reflectors (DABRs) in the experimental structure. Layers of alternating materials with contrasting acoustic impedances embedded a wavelength away from the surface serve to reflect energy back to the surface. Using numerical simulations, we show that a single Bragg reflector is sufficient to increase the energy density at the surface by more than five times. We quantify the resulting damping time to find that it is longer than the intrinsic damping time. The proposed structure can enable future measurements of intrinsic damping in SAWs at $\sim$100 GHz.

To my parents, for their love and support.

ACKNOWLEDGMENTS

I would like to express my sincere gratitude to my adviser Professor Sanjiv Sinha, who gave me the freedom to choose topic I was interested in and guided me through the research work from scratch. I am very fortunate to have learned an eloquent writing and presentation style from him. His advice on personal development and understanding of my situation as an international student have been of tremendous help.

This work could not be finished without my collaborators. Special acknowledgements to Dr. Jyothi Sadhu, who helped me begin and pursue successfully a great deal of the project. I would wish to thank Dr. Marc Ghossoub for his constructive criticism and suggestions on improving the rigor of my research . I owe my thanks to Dr. Jun Ma and Krishna Valavala, who taught me cleanroom skills and shared interesting ideas regarding device fabrication. Finally, I want to thank my parents who have been very supportive of my decision to go to a graduate school.

TABLE OF CONTENTS

LIST OF TABLES vi

LIST OF FIGURES vii

CHAPTER 1 INTRODUCTION 1
1.1 Background and Motivation 1
1.2 Structure of the Thesis 3

CHAPTER 2 COMPARISON OF DISSIPATION MECHANISMS 4
2.1 Intrinsic Mechanisms 4
2.1.1 Phonon-phonon interaction 4
2.1.2 Thermoelastic Damping 5
2.1.3 Phonon-electron Interaction 7
2.2 Extrinsic Mechanisms 7
2.2.1 Bulk Radiation 7
2.2.2 Surface Scattering 11
2.3 Overall Damping 11

CHAPTER 3 DISTRIBUTED ACOUSTIC BRAGG REFLECTOR (DABR) 14
3.1 Theoretical Background 14
3.2 Finite Element Calculations 15

CHAPTER 4 CHARACTERIZATION OF NON-IDEAL DEVICES 24

CHAPTER 5 SUMMARY AND CONCLUSIONS 28

REFERENCES 29

LIST OF TABLES

3.1 Acoustic properties for some common bulk materials[1]. 15

LIST OF FIGURES

2.1 (Inset) Damping times of SAWs at different duty cycle calculated analytically (solid line) and using finite element simulations (dashed line). The data is adapted from Ref. [2]. All calculations are for aluminum gratings on silicon substrates with periodicity, $p = 400$ nm. 9

2.2 Surface energy fraction calculated at different duty cycles, η using finite element simulations. The peak corresponds to the frequency of the SAW in each case. 10

2.3 Damping times associated with different dissipation mechanisms. We assume the SAW to be generated using an aluminum grating on silicon. The thickness of the metal is 40 nm and the duty cycle is 0.8. 12

3.1 Schematic of the structure showing Bragg layers sandwiched in a silicon substrate. The period, p of the grating is 300 nm and the height of the aluminum film, h is 40 nm. The thicknesses of the tungsten and SiO_2 films are 75 nm each. 18

3.2 Displacement fields for different normal modes (at phase angle, $\phi = 0$) with (a) odd and (b) even symmetry. White dotted lines represent the undeformed edge of the structure. Displacement amplitudes are magnified to reveal the difference between the deformed and the undeformed configurations of the structure is visible. 20

3.3 Kinetic energy density of the normal mode (at $\phi = 0$) corresponding to the SAW for a structure (a) without and (b) with a DABR. The amplitudes of kinetic energy density are magnified. 21

3.4 Surface energy fraction for SAWs excited with and without a DABR. The calculations are for a grating period, $p = 300$ nm that corresponds to a SAW of ~ 14 GHz. 22

3.5 Ideal quality factor for a SAW resonator calculated with and without a DABR. The calculations are for a grating period, $p = 300$ nm that corresponds to a SAW of ~ 14 GHz. 23

4.1 Kinetic energy density of the normal mode (at $\phi = 0$) corresponding to the SAW with the following thicknesses of tungsten and SiO_2 films: (a)75 nm and 75 nm (b) 90 nm and 75 nm (c) 75 nm and 90 nm (d)60 nm and 90 nm Amplitude of kinetic energy density have been magnified. 25

4.2 Kinetic energy density of the normal mode (at $\phi = 0$) corresponding to the SAW with different depths of silicon device layer: (a) $d = p$ (b) $d = 2p$ (c) $d = 3p$. Amplitude of kinetic energy density have been magnified. 26
4.3 Kinetic energy density of the normal mode (at $\phi = 0$) corresponding to the SAW with (a) single crystal and (b) polycrystalline silicon device layer. Amplitude of kinetic energy density have been magnified. 27

CHAPTER 1

INTRODUCTION

1.1 Background and Motivation

Surface acoustic waves (SAWs) find use in diverse applications[3] from radar and communication systems to consumer electronics to non-destructive evaluation. The attenuation of SAWs has been extensively studied in the low-frequency regime ($\sim$MHz)[4] where most SAW filters operate. Higher frequency ($\sim$1-100 GHz) SAWs are important for sensing mass change, liquid density and temperature, and for probing semiconductor surfaces. Measured lifetimes, however decrease rapidly from $\sim$9 ns at $\sim$6 GHz[5] to $\sim$60 ps at $\sim$48 GHz[6]. Improving lifetimes beyond these figures requires a thorough quantification of diverse damping mechanisms and a direct measurement of intrinsic limits to damping at high frequencies. Despite fundamental understanding of intrinsic (such as thermoelastic[7], Landau-Rumer[8] and Akhiezer [9]) damping mechanisms, little experimental data is available to quantify the intrinsic limits on damping of SAWs at $\gtrsim$GHz frequencies.

Existing experimental literature on intrinsic dissipation mechanisms[10, 11] almost exclusively focuses on bulk longitudinal or transverse acoustic phonons. For example, the effect of Akhiezer and thermoelastic damping[12, 13, 14] on the lifetimes of longitudinal and transverse waves in dielectric materials has been extensively studied. Attenuation contributed

by both mechanisms depends on the polarization of the phonon. Recent measurements on the attenuation of 50 and 100 GHz longitudinal acoustic modes in silicon[15] show that Akhiezer is the dominant mechanism at 300 K. In comparison, quantitative measurements on the intrinsic damping of SAWs are relatively unexplored. The temperature and frequency dependence of attenuation for SAWs are expected to be markedly different[7, 8] from that of longitudinal or transverse phonons. While guidance from theory exists for several damping mechanisms[7, 8, 16], their reliability is largely untested.

Generally, GHz high-frequency SAWs are generated using femtosecond laser absorption in metallic gratings on substrates [17, 18, 19, 20, 21] that are usually non-piezoelectric. While recent work[5, 22] has established the dynamics in the generation process, a complete quantitative understanding of attenuation is still lacking. In the typical pump-probe experiment, all mechanisms are simultaneously active. Distinguishing between extrinsic and intrinsic damping in existing measurements remains challenging. In this paper, we use theory to quantitatively compare damping times for thermoelastic dissipation, Akhiezer damping, phonon-electron scattering and extrinsic mass loading respectively. We find that extrinsic damping due to mass loading dominates SAW attenuation in the 1-100 GHz range. The mechanism is progressively dominant at higher frequencies.

Experimental structures that are relatively insensitive to mechanical loading are necessary to measure intrinsic damping. Here, we propose structures with alternating material layers of contrasting acoustic impedances sandwiched in the substrate. These layers act as distributed acoustic Bragg reflectors (DABRs) and reflect the energy dissipated into the bulk, back to the surface. The reflection confines energy in the SAW to the surface and greatly limits

dissipation from mechanical loading. We show that the introduction of even a single-layer DABR reduces extrinsic damping by at least an order of magnitude. From our calculations, the reduction of extrinsic damping is sufficient to allow intrinsic damping mechanisms to dominate. We therefore anticipate that measurements on the proposed structure can provide quantitative insight into intrinsic damping.

1.2 Structure of the Thesis

The rest of the thesis is organized as follows.

In Chapter 2, we present a theoretical formulation of damping caused by different dissipation mechanisms. In particular, we explore the frequency dependence of the damping time, τ for each mechanism and compare damping times due to different dissipation mechanisms across the GHz range. We rely on previous theory for intrinsic mechanisms and mainly focus on extrinsic mechanical loading. We conclude that mechanical loading is the dominant mechanism.

In Chapter 3, we use finite element calculations to quantify the improvement in the damping time of a GHz SAW in the presence of a DABR. This work outlines a rational design of experimental structures that can enable a comprehensive study of the effect of intrinsic damping mechanisms in surface acoustic phonons in the $\sim$1-100 GHz range.

Finally, we summarize the theoretical and computational findings in Chapter 4.

CHAPTER 2

COMPARISON OF DISSIPATION MECHANISMS

In this section, we briefly review the key attenuation mechanisms that are relevant to this work. We assume that the SAW is generated by ultrafast laser illumination of a metallic grating on a non-piezoelectric substrate[5, 2]. We further assume a clean surface and ignore attenuation due to surface impurities/defects of any kind except nominal surface roughness. Intrinsic damping mechanisms have been studied in detail previously[23, 24, 9, 15, 7, 25]. Here, we retrace the relevant ones for completeness and then consider the extrinsic mechanism of mass loading in depth.

2.1 Intrinsic Mechanisms

2.1.1 Phonon-phonon interaction

The attenuation of high frequency ultrasound in dielectric crystals due to interaction with thermal phonons has been reviewed[23] in detail. There are two distinct approaches to model the interaction of surface acoustic phonons with thermal phonons. In the Landau-Rumer model[24], the interaction of thermal and acoustic phonons proceeds via anharmonic three phonon scattering. This is valid when $\omega\tau_{th} >> 1$, where ω is the angular frequency of the acoustic wave and τ_{th} is the average thermal phonon relaxation time. In the alternate

Akhiezer model [9], the SAW acts as a driving force to perturb the equilibrium population of thermal phonons. The collisions of non-equilibrium phonons increases entropy and removes energy from the original wave. This approach is valid when $\omega << \frac{k_B T}{\hbar}$ where, k_B is Boltzman's constant, T is the temperature and $k_B T/\hbar$ is the average thermal phonon frequency. It is difficult to demarcate the frequency at which the Akhiezer regime should cross over to the Landau-Rumer regime. The main difficulty lies in estimating the average thermal relaxation time. For silicon at room temperature, the average thermal phonon relaxation time, τ_{th} is estimated to be tens of picoseconds[15]. Since we are primarily interested in ∼1-100 GHz frequencies, the appropriate condition is $\omega\tau_{th} \sim 1$ and therefore, Akhiezer's model appears to be the correct choice. A simplified expression for calculating the attenuation τ due to Akhiezer mechanism is given by [15]

$$\tau^{-1} = \frac{CT}{\rho {V_L}^2} \frac{\omega^2 \tau_{th}}{1 + \omega^2 \tau_{th}^2} (< \gamma^2 > - < \gamma >^2), \tag{2.1}$$

where C is the volumetric heat capacity, V_L is the longitudinal wave speed, γ is the grüneisen parameter and $<>$ denotes an average over all modes.

2.1.2 Thermoelastic Damping

The attenuation of elastic surface waves propagating on a dielectric crystal due to thermoelastic damping has been previously studied[7]. Here, we simplify the results for a Rayleigh wave traveling on an isotropic substrate. Thermoelastic damping is different from Akhiezer in that phonons achieve equilibrium through spatial redistribution rather than through Normal and Umklapp processes. A SAW passing through a solid creates regions of opposite

strain. The compressed regions become hotter compared to the expanded regions which results in diffusive transport of heat between the two. The irreversible flow of heat removes energy from the wave. In order to estimate the attenuation due to heat conduction, we first consider the governing equations of thermoelasticity

$$\sigma_{ij} = L\epsilon_{kk}\delta_{ij} + 2G\epsilon_{ij} - \beta\delta_{ij}\theta, \tag{2.2}$$

$$\rho C_v\dot{T} + 3B\alpha T_o\dot{\epsilon_{ii}} = k\nabla^2 T, \tag{2.3}$$

where σ_{ij}, ϵ_{ij} are the components of stress and strain tensor, L is the *Lamè* parameter, G is the shear modulus, $\theta = T - T_o$ is the excess temperature, ρ is the density, C_v is the specific heat at constant volume, B is the bulk modulus, k is the thermal conductivity and $\beta = \alpha E/(1-2\nu)$. Here, α is the thermal expansion coefficient, E is the Young's modulus, and ν is the Poisson's ratio. The average rate of entropy production resulting from heat flux, $\mathbf{h}$ is

$$\dot{S} = -\int < \frac{\nabla\cdot\mathbf{h}}{T_o + \Delta T} > dV = \int < \frac{k\nabla^2 T}{T_o + \Delta T} > dV. \tag{2.4}$$

We can evaluate the above expression for entropy generation from Eq. (2.2) and Eq. (2.3)[7]. The rate at which energy is dissipated is given by

$$P_{th} = T\dot{S} = -\frac{9TkB^2\alpha^2}{2\rho^2 C_v^2}\int < \epsilon_{ii}\nabla^2\epsilon_{ii} > dV. \tag{2.5}$$

2.1.3 Phonon-electron Interaction

Another mechanism for attenuation is the interaction of surface acoustic phonons with conduction electrons inside the metallic structures. At low frequencies, when the electron mean free path, Λ is much smaller than the acoustic wavelength, λ, we can simplify Pippard's [25] formulation to evaluate the attenuation caused by phonon-electron interactions as

$$\tau^{-1} = \frac{2n_e m_e v_F^2 \omega^2 \tau_e}{15\rho V_L^2}, \tag{2.6}$$

where n_e is the number of free electrons per unit volume, m_e is the rest mass of an electron, v_F is the Fermi velocity and τ_e is the relaxation time of the electron.

2.2 Extrinsic Mechanisms

2.2.1 Bulk Radiation

Amongst extrinsic damping, the primary one is that due to mass loading from the metallic grating patterned on the substrate. In experiments, the grating is illuminated by an ultrashort laser pulse. Disparate absorption between the grating and the substrate causes expansion of the metal leading to a non-zero stress at the metal-substrate interface. The normal component of this stress forces the metal to follow the motion of the surface. The equation of motion is given by

$$\rho_M \frac{\partial^2 u_z}{\partial t^2} = \frac{\partial \sigma_{zz}}{\partial z}, \tag{2.7}$$

where ρ_M is the density of the metal, σ_{zz} is the normal component of the stress tensor at the interface, and u_z is the displacement of the surface in the z-direction. If the thickness, w_M of the metallic grating is small, the displacement in the grating can be assumed to be constant. Therefore, σ_{zz} can be estimated from Eq. (2.7) as [26]

$$\sigma_{zz} = \rho_M w_M u_z \omega^2. \tag{2.8}$$

The above stress has the same spatial period as the grating and therefore can be spectrally decomposed into components with wavenumbers $2\pi n/p$, where p is the periodicity of the grating and n is an integer. It has been previously shown [19, 26] that only the $n = 0$ component radiates energy into the bulk. We calculate the rate of radiation per unit area for a given grating using the $n = 0$ component and applying Poynting's theorem

$$\frac{dE}{dt} = \frac{\rho_M^2 w_M^2 \omega^4 u_{z0}^2 (1 - cos(2\pi\eta))^2}{8\pi^2 V_L \rho_s}, \tag{2.9}$$

where η is the fraction of the substrate surface covered with metal (duty cycle), ρ_s is the density of the substrate and u_{z0} is the maximum displacement at the surface.

Equation (2.9) reveals that radiation of energy into the bulk depends on the duty cycle of the grating. If there were no metallic grating, the SAW would exist as an eigenmode of the system and no radiation should be expected. Conversely, if the entire surface is covered with the metal, there would be a shift in the velocity of the SAW but energy would again not be dissipated into the bulk. Theory predicts maximum damping at $\eta = 0.5$, which is in agreement with experimental data[2], as shown in Fig. 2.1 and discussed below.

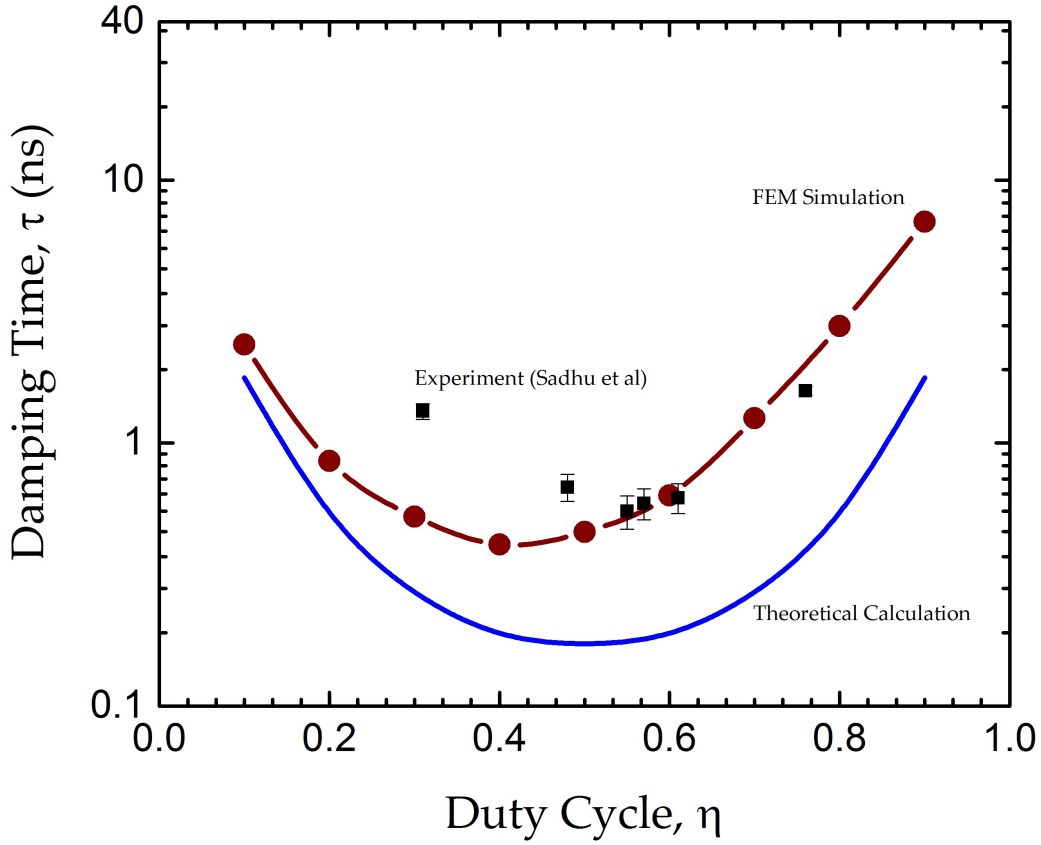


Figure 2.1: (Inset) Damping times of SAWs at different duty cycle calculated analytically (solid line) and using finite element simulations (dashed line). The data is adapted from Ref. [2]. All calculations are for aluminum gratings on silicon substrates with periodicity, p = 400 nm.

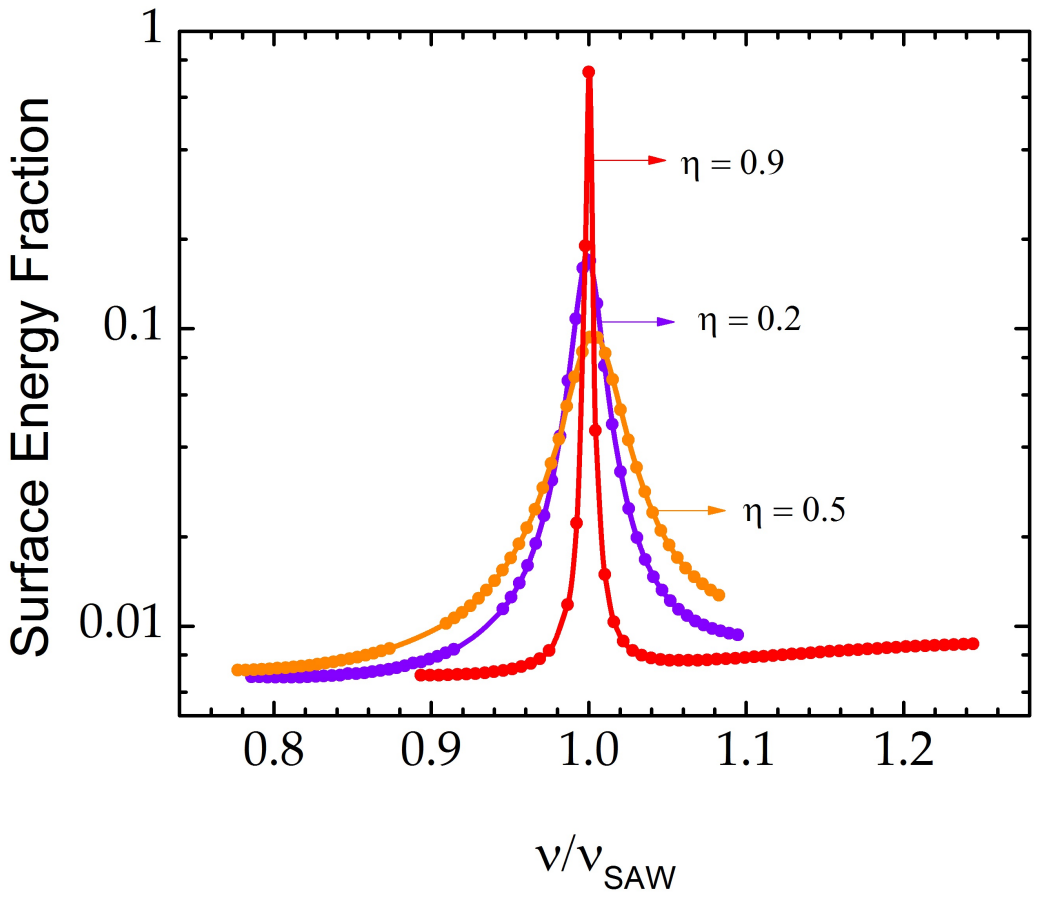


Figure 2.2: Surface energy fraction calculated at different duty cycles, η using finite element simulations. The peak corresponds to the frequency of the SAW in each case.

Figure 2.2 plots the surface energy fraction at different duty cycles. We define the surface energy fraction as the fraction of kinetic energy confined within one wavelength from the surface. Fig. 2.1 is the variation in damping time with duty cycle. We show both the analytical result (solid line) from above, and a more exact finite element calculation (dashed line) without using a thin film approximation. The trend is similar in both cases though the finite element calculations agree better with experimental data. We note that the analytical theory predicts the order of magnitude of the damping time correctly.

2.2.2 Surface Scattering

Roughness of the surface also serves to attenuate SAWs. The height of the surface above an average (x, y) plane is given by the function $f(x, y)$ where $< f(x, y) >= 0$ and $< f(x, y)^2 >= \delta^2$. We assume that the correlation between two points on the surface follows Gaussian statistics such that $< f(0)f(r_{xy}) >= \delta^2 \exp(-{r_{xy}}^2/a^2)$ where a is the roughness correlation length. The attenuation coefficient has been derived previously in detail and is given by[27]

$$\tau^{-1} = \frac{\delta^2 a^2}{\pi} \left(\frac{\omega}{V_R} \right)^5 F(x), \tag{2.10}$$

where V_R is the Rayleigh speed of the wave and the function F depends only on material properties when the wavelength of the SAW is longer than the correlation length. The latter condition is typical in experiments. In our calculations, we assume typical surface roughness parameters for cleanroom processed silicon surface, with $\delta \sim$1 nm and $a \sim$ 15 nm[28].

2.3 Overall Damping

The total attenuation for a SAW is a summation over individual dissipation mechanisms. Figure 2.3 compares the magnitudes of damping time associated with each dissipation mechanism. The damping due to extrinsic mass loading from the grating emerges as the dominant mechanism across the 1-100 GHz range. Mass loading has a strong dependence on frequency ($\sim \omega^4$). In the GHz regime, this is the dominant attenuation. Above 10 GHz, this attenuation exceeds others by more than an order of magnitude. While the exact magnitudes

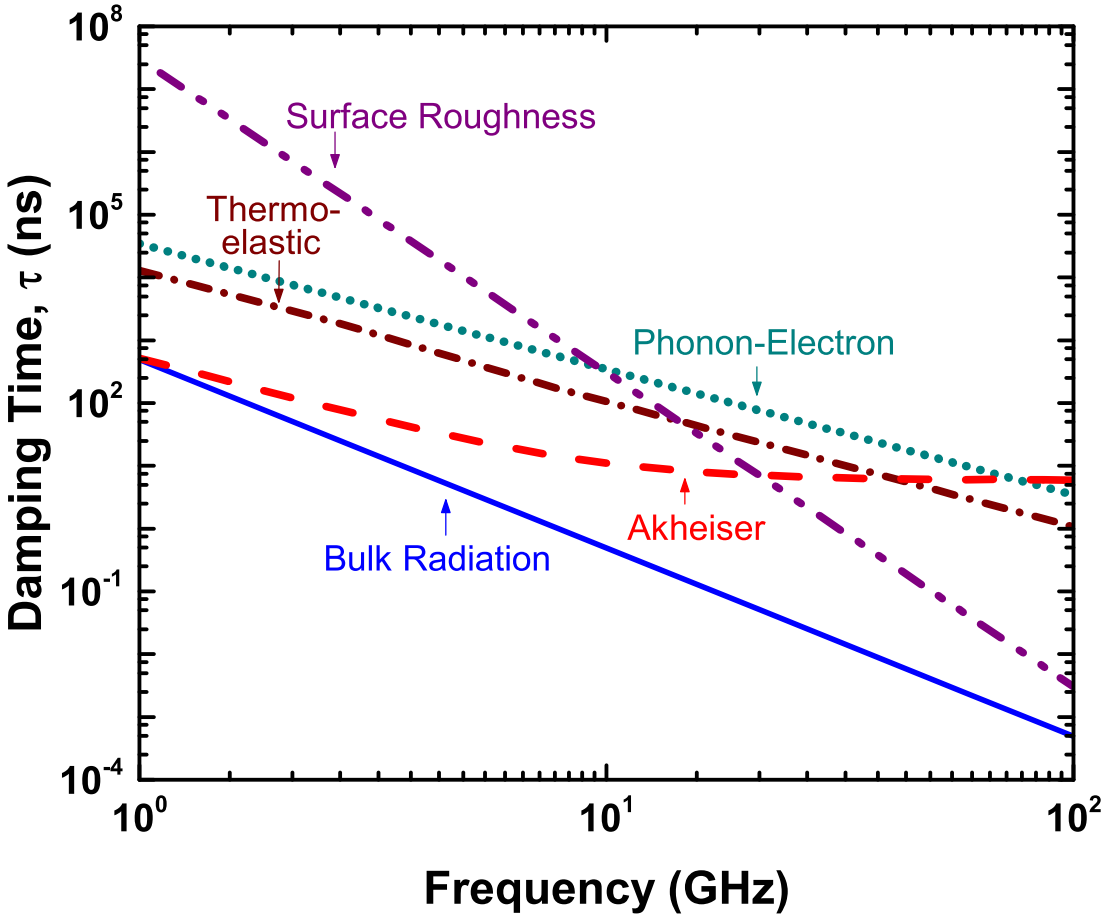


Figure 2.3: Damping times associated with different dissipation mechanisms. We assume the SAW to be generated using an aluminum grating on silicon. The thickness of the metal is 40 nm and the duty cycle is 0.8.

depend on the size of the grating and the choice of metal/substrate, the overall trend will be similar for other structures due to the strong frequency dependence for mass loading. We conclude that experiments employing gratings to generate SAWs in the GHz range only measure the damping time associated with extrinsic mass loading.

CHAPTER 3

DISTRIBUTED ACOUSTIC BRAGG REFLECTOR (DABR)

3.1 Theoretical Background

As discussed above, SAWs generated through optical excitation of patterned metallic gratings are damped dominantly due to radiation of energy into the bulk. In this section, we propose an experimental structure that mitigates damping due to extrinsic mass loading and should enable direct measurements of the intrinsic dissipation of SAWs.

We first note some qualitative features of the bulk radiation. Since SAWs are excited using a metallic grating with a period p, the resulting radiation must have a wave vector whose component along the propagation direction (assumed to be x-) should be an integral multiple of $2\pi/p$ and satisfy

$$\omega = V_{L(T)}\sqrt{k_z^2 + (\frac{2\pi n}{p})^2}, \tag{3.1}$$

where k_z is the wavevector in the z-direction (into the depth), n is an integer and $V_{L(T)}$ is the speed of longitudinal (or transverse) waves. Since, dissipation only occurs for $n = 0$, the radiation of energy into the substrate occurs at normal incidence.

The propagation direction can be exploited to significantly reduce the damping through the use of distributed acoustic Bragg reflectors (DABRs). A DABR consists of multiple layers

of alternating materials with contrasting acoustic impedances ($Z = \rho V_L$). Each layer causes partial reflection of the dissipated radiation such that the reflections combine constructively at the surface. Table 1 lists the acoustic impedances of some common materials that can be used for Bragg layers. Among these, the greatest contrast in acoustic impedances arises between tungsten ($Z = 101$) and SiO_2 ($Z = 12.5$) due to a large difference in density. We note that Table I lists bulk properties and the properties for thin films may vary depending on deposition conditions. We find the impact of this variation to be insignificant and discuss it later.

Table 3.1: Acoustic properties for some common bulk materials[1].

Material	Longitudinal Speed (m/s)	Transverse Speed (m/s)	Density (g/cm^3)	Acoustic Impedance (MRayls)
Tungsten	5200	2900	19.4	101
Nickel	5600	3000	8.8	49.5
Copper	5010	2270	8.9	44.6
Silicon	8430	5840	2.3	19.7
Aluminium	6420	3040	2.7	17.3
Silica	5700	3750	2.2	12.5

3.2 Finite Element Calculations

We now compute improvements in the damping time in the presence of a DABR. Figure 3.1 shows a schematic of the DABR structure. The structure consists of alternating layers of tungsten and SiO_2 sandwiched inside silicon. Acoustic energy dissipated into the bulk is incident at the interface with tungsten and is separated into reflected and transmitted components. The transmitted component travels through the SiO_2 layer and is reflected and transmitted again at the interface with the next Bragg layer. This is repeated at every

interface and the fraction of energy reflected due to each Bragg layer is a summation over all the reflections.

The thicknesses (δx) of the layers (W/SiO_2) is important in the performance of the DABR. Based on wave propagation theory, we expect maximum reflection when the thickness of each layer is chosen to produce a phase shift of a quarter of the wavelength ($\omega \delta x = V_L \pi/4$). The phase shift criteria requires the two alternating materials to have different thickness if they have different acoustic velocities. However, for materials such as tungsten and SiO_2, the acoustic velocity differs only by 8 percent and therefore, the thicknesses of the two layers may be assumed to be the same. To obtain an approximate estimate of the efficacy of the Bragg layers, we can evaluate the reflection coefficients[29] based on acoustic impedances. Since the mismatch in acoustic impedances between tungsten and SiO_2 is large, a single-layer appears sufficient in reflecting most of the radiant energy back to the surface. An analysis reveals a broadband of frequencies ($0.75 < \nu/\nu_{SAW} < 1.75$) over which the reflected energy is $\gtrsim$95 percent. There is only a marginal increase in the fraction of energy reflected when increasing the number of Bragg layers from one to two.

We now employ numerical calculations to further quantify damping in the presence of a single Bragg reflector. The system is modeled as a continuum composite of a silicon substrate with an aluminum grating on top, as depicted in Fig. 3.1. The individual metal lines have width d and height h. The depth of the silicon device layer between the grating and the Bragg layers is considered to be the same as the periodicity of the grating. To model experimental conditions, the height of the metal is chosen to be 40 nm. We choose a grating period of 300 nm that corresponds approximately to 14 GHz. The thicknesses of the

tungsten and the SiO_2 films are chosen to be one-quarter wavelength or 75 nm each. The elastic equation of motion governing the displacement $\mathbf{u(t)}$ of the system is given by

$$\partial_j[c_{ijmn}\mathbf{(r)}\partial_n u_m] = \rho(\mathbf{r})\ddot{u}_i, \tag{3.2}$$

where $\rho(\mathbf{r})$ and $c_{ijmn}(\mathbf{r})$ are the position dependent mass and elastic stiffness tensor. For simulation purposes, all the materials are assumed to be isotropic. To extract the normal modes of this structure, we assume $\mathbf{u(t)}$ to have a harmonic dependence ($e^{i\omega t}$) and insert it into Eq. (1)

$$\partial_j[c_{ijmn}\mathbf{(r)}\partial_n u_m] = -\rho(\mathbf{r})\omega^2 u_i. \tag{3.3}$$

We solve the eigenvalue problem using the finite element method (FEM) on ANSYS[30]. Figure 3.1 shows the simulated unit cell. We employ meshes with 2-D structural solid elements that possess 4 nodes. The elements have two degrees of freedom at each node: translations in the x- and the z- directions. Since the thickness of the substrate is very large compared to the wavelength, λ as well as the dimensions of the grating, a zero displacement boundary condition is used at the bottom. In order to simulate the entire composite from this unit cell, a periodic Bloch condition ($u_1 = u_2 e^{ik_x p}$) is chosen for the sides. All calculations are performed at $k_x = 0$ and $p = \lambda$, corresponding to the first harmonic at the center of the surface Brillouin zone. The mesh size determines the convergence and accuracy for the solution obtained using FEM. Since the displacement field for a SAW is mostly near the surface, the region comprising the aluminum grating, the top silicon and the Bragg layers

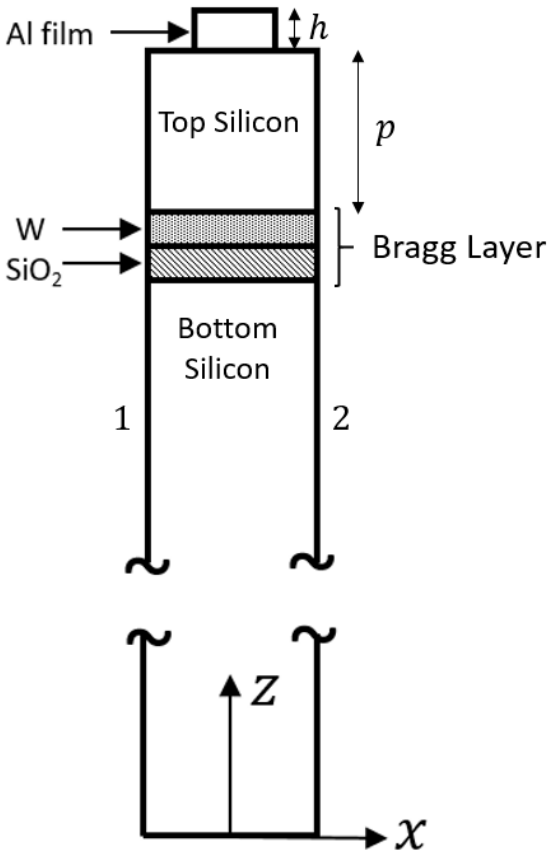


Figure 3.1: Schematic of the structure showing Bragg layers sandwiched in a silicon substrate. The period, p of the grating is 300 nm and the height of the aluminum film, h is 40 nm. The thicknesses of the tungsten and SiO_2 films are 75 nm each.

requires a fine mesh. A coarser mesh is adopted for the remaining bulk of the substrate to decrease computation time. We performed a mesh sensitivity analysis by reducing the size of elements and monitoring the change in the frequency of normal modes. We found that elements with sizes of 8 nm and 120 nm for the fine and the coarse mesh respectively are sufficient for our calculations. We extract the normal modes of the system in the desired frequency range using the Block Lanczos method. The convergence criteria is that the normalized change in the frequency of normal modes between successive iterations is less than 10^{-5}.

Modes obtained using this method may possess an odd or an even symmetry in their displacement fields as shown in Fig. 3.2. To further select the excited mode, we note that the heating from the laser possesses radial symmetry. The initial excitation of the system should also exhibit even symmetry and therefore, modes with odd displacement profiles cannot be excited. We only consider solutions with even symmetry. The probability of excitation for a particular mode is proportional to the concentration of energy at the surface for that mode. A surface mode is identified as possessing the maximum surface energy fraction amongst the different modes. As previously noted, the surface energy fraction is defined as the fraction of energy present within one wavelength from the surface. The quality factor is then the full width at half maximum (FWHM) of the distribution around the peak frequency.

Figure 3.3 compares the kinetic energy density field with and without a DABR. In Fig. 3.3(a), without a DABR, surface modes are coupled to bulk modes which enables leakage of energy into the bulk. The use of the DABR clearly confines energy at the surface, as shown in Fig. 3.3(b). Figure 3.4 further compares the fraction of energy confined to the

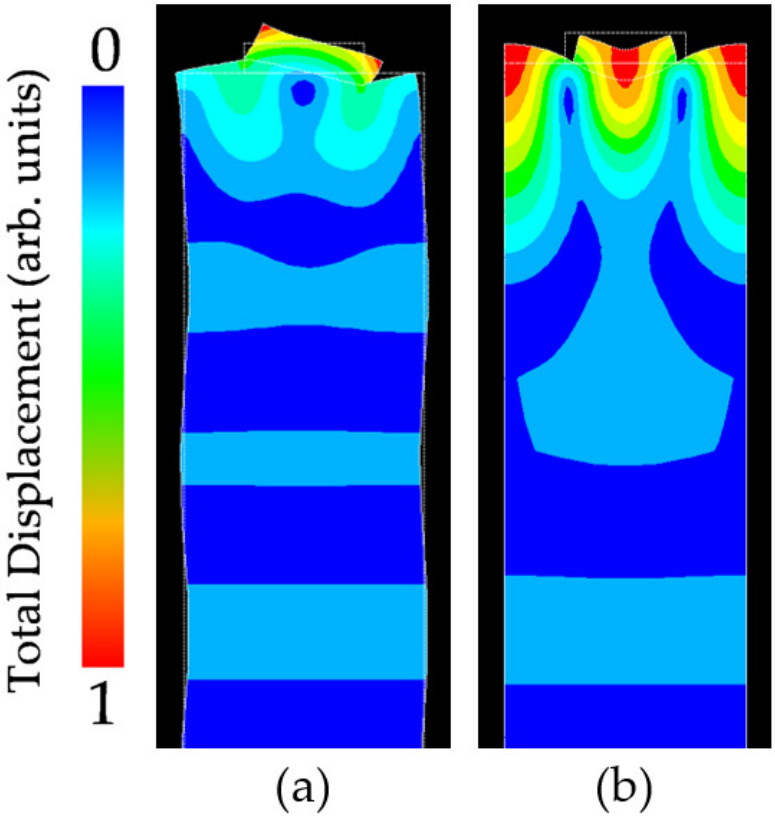


Figure 3.2: Displacement fields for different normal modes (at phase angle, $\phi = 0$) with (a) odd and (b) even symmetry. White dotted lines represent the undeformed edge of the structure. Displacement amplitudes are magnified to reveal the difference between the deformed and the undeformed configurations of the structure is visible.

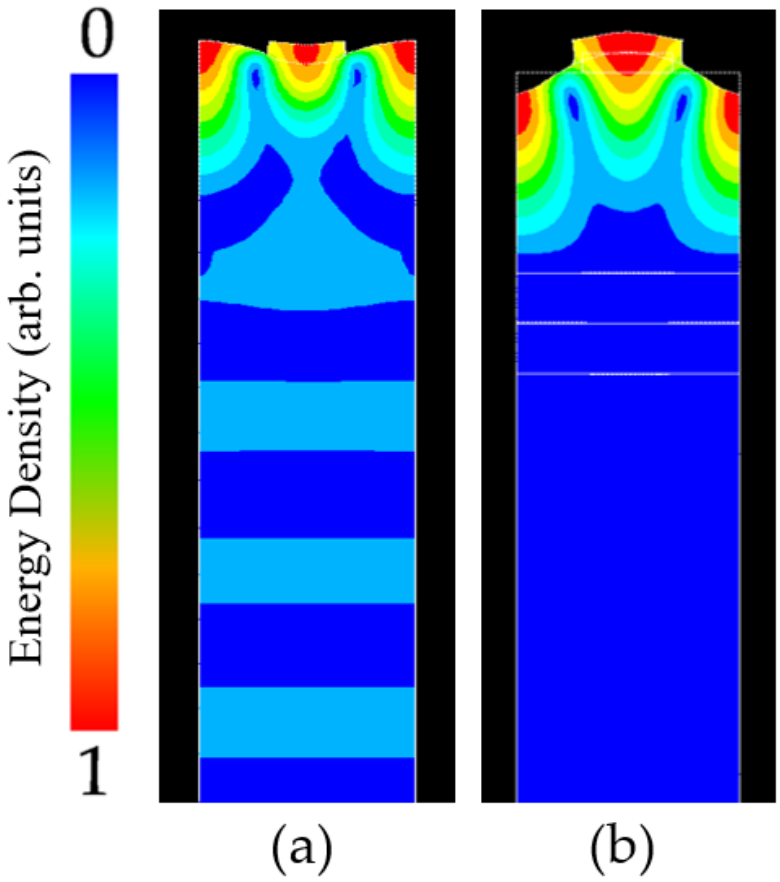


Figure 3.3: Kinetic energy density of the normal mode (at $\phi = 0$) corresponding to the SAW for a structure (a) without and (b) with a DABR. The amplitudes of kinetic energy density are magnified.

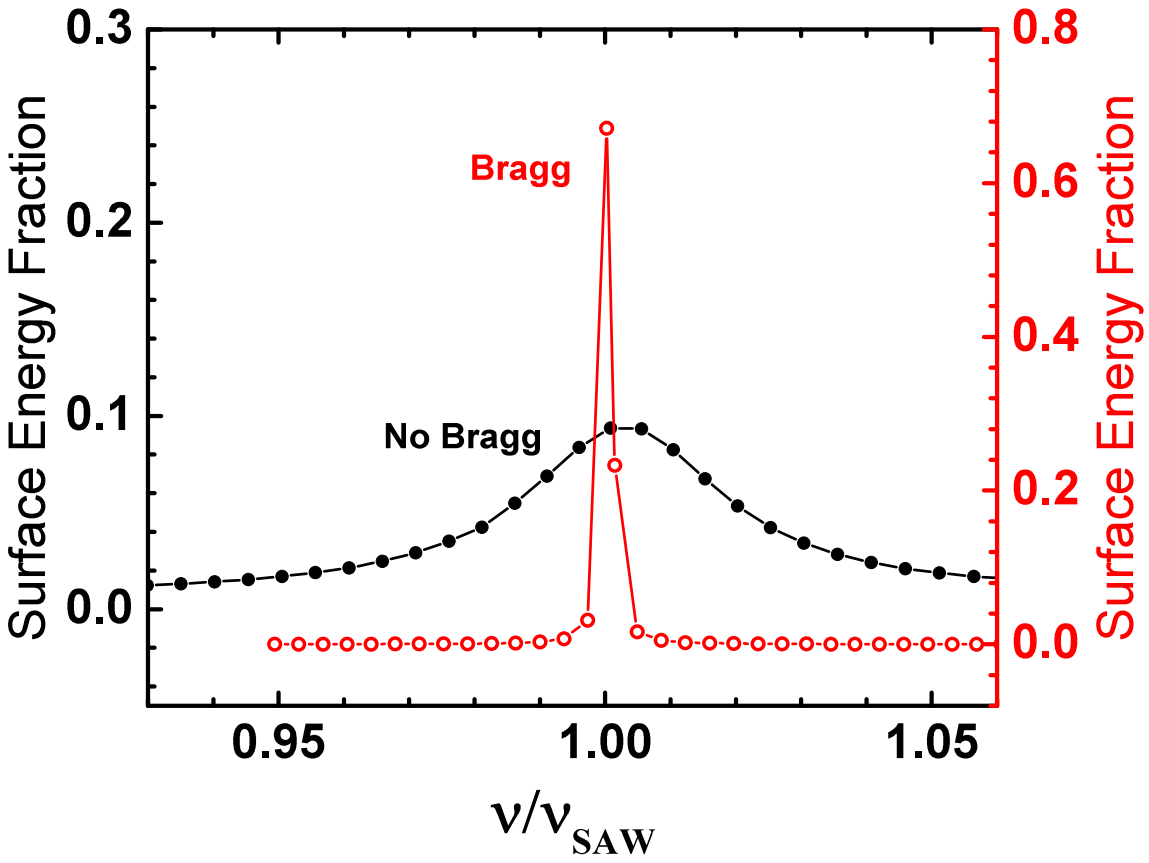


Figure 3.4: Surface energy fraction for SAWs excited with and without a DABR. The calculations are for a grating period, $p = 300$ nm that corresponds to a SAW of ~ 14 GHz.

surface with and without a DABR. In the normal experimental situation without a DABR, the surface energy fraction is ∼12 %. This increases to ∼70 % with the use of a single DABR layer.

Indeed the peak in the surface energy fraction with a DABR is too sharp to enable us to accurately estimate the quality factor from our simulations. Here we provide a lower side estimate of the quality factor. At a duty cycle, $\eta = 0.5$, the quality factor, Q associated with extrinsic mass loading improves from 30 to 637 with a DABR, a factor >20 as shown in Fig. 3.5. This corresponds to a damping time of 22 ns for the SAW at 14 GHz. This is a

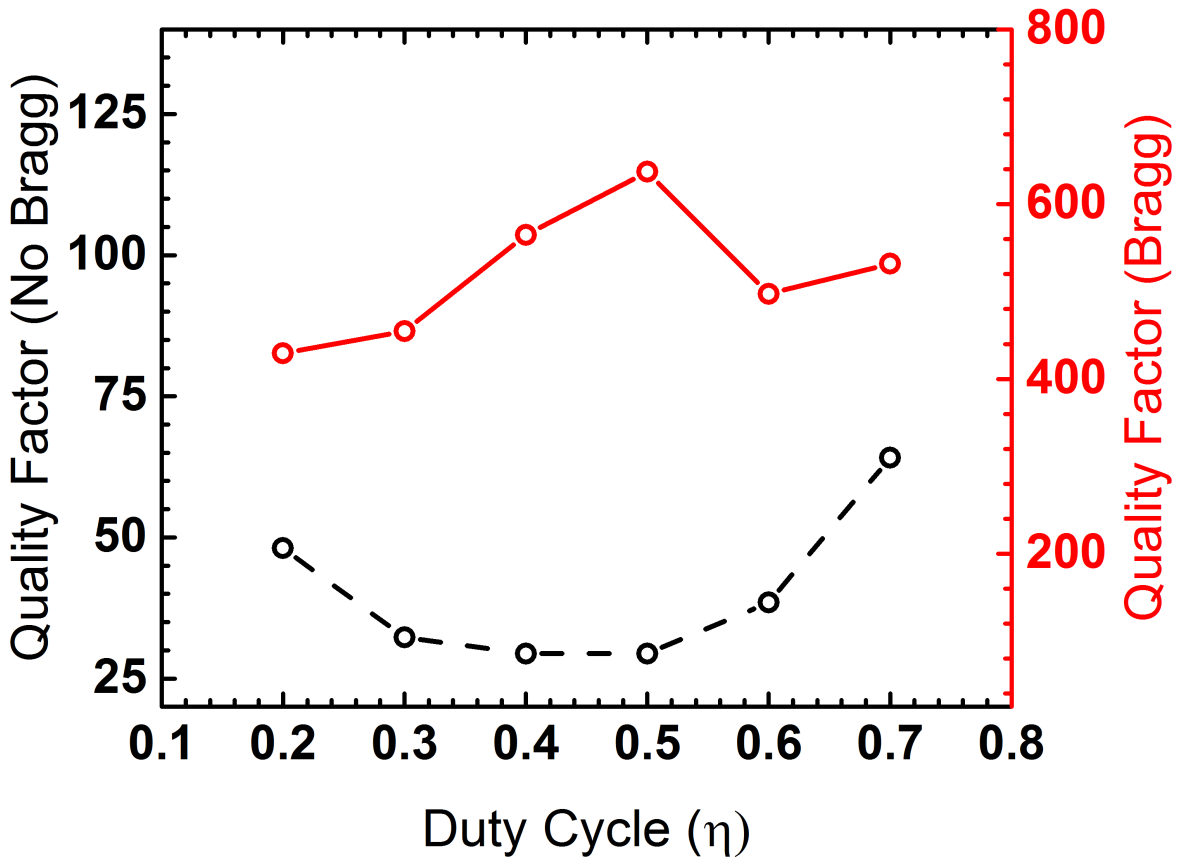


Figure 3.5: Ideal quality factor for a SAW resonator calculated with and without a DABR. The calculations are for a grating period, $p = 300$ nm that corresponds to a SAW of ~ 14 GHz.

higher side estimate of the damping, and we expect the actual damping time to be possibly lower in the presence of the DABR. In comparison, we estimate the damping time for the Akhiezer process to be 8 ns.

CHAPTER 4

CHARACTERIZATION OF NON-IDEAL DEVICES

In practice, experimental structures incorporating DABRs will likely not be as ideal as the ones considered thus far. Non-ideality can stem from actual layer thicknesses being different from the design figures. Further, material properties are known to differ from the bulk in thin films depending on growth/fabrication conditions. In particular, the top layer silicon is likely to be polycrystalline. We have investigated whether such non-idealities affect the functioning of the DABR. First, we find that the confinement of SAW energy at the surface is reasonably insensitive to changes in the layer thicknesses of DABR materials for changes of as much as 20% from the design values as shown in Fig. 4.1. We find that SAWs are essentially similarly confined in all cases. Thus, the influence of the Bragg layers is not overtly sensitive to the exact thicknesses of the layers within reasonable bounds.

The thickness of the top (device) layer affects the performance of the DABRs in a different manner. In our previous calculations, we assumed the thickness of the silicon device layer to be the same as the periodicity, p of the grating. We now consider thicknesses of the silicon device layer to be twice and thrice the periodicity respectively. Figure 4.3 plots the kinetic energy density field for the SAW in each case. While the energy of the SAW is still confined to the device layer in each case, the surface energy fraction (within a depth of one wavelength) reduces as the device layer is made thicker. On the other hand, choosing a sub-

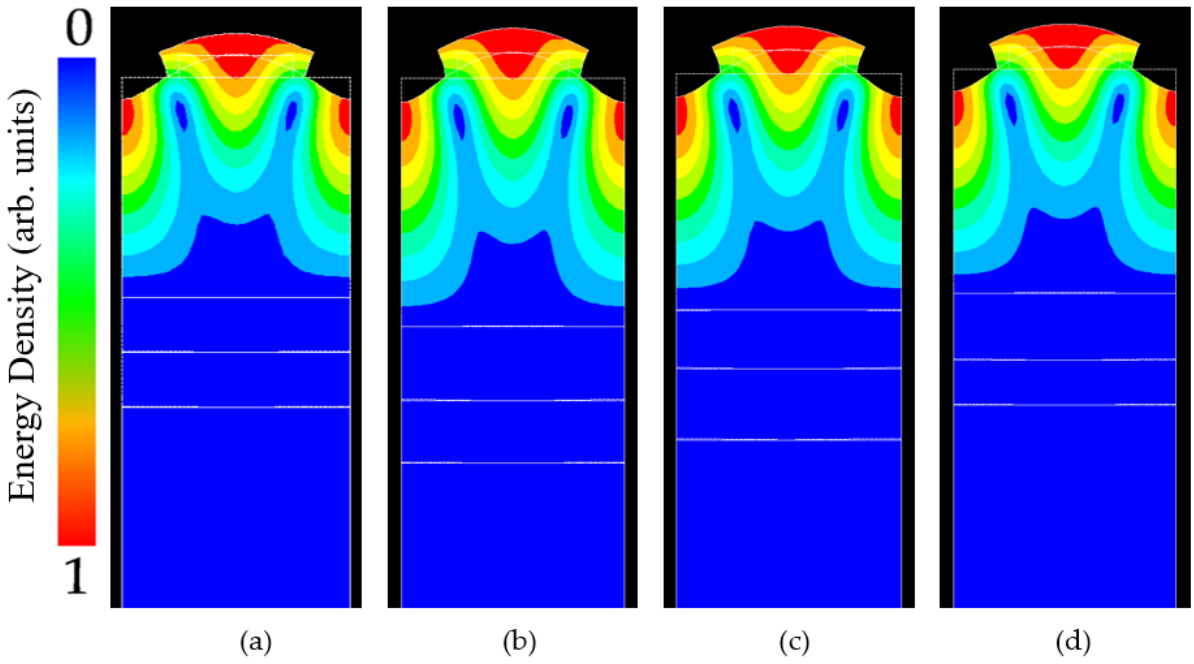


Figure 4.1: Kinetic energy density of the normal mode (at $\phi = 0$) corresponding to the SAW with the following thicknesses of tungsten and SiO_2 films: (a)75 nm and 75 nm (b) 90 nm and 75 nm (c) 75 nm and 90 nm (d)60 nm and 90 nm Amplitude of kinetic energy density have been magnified.

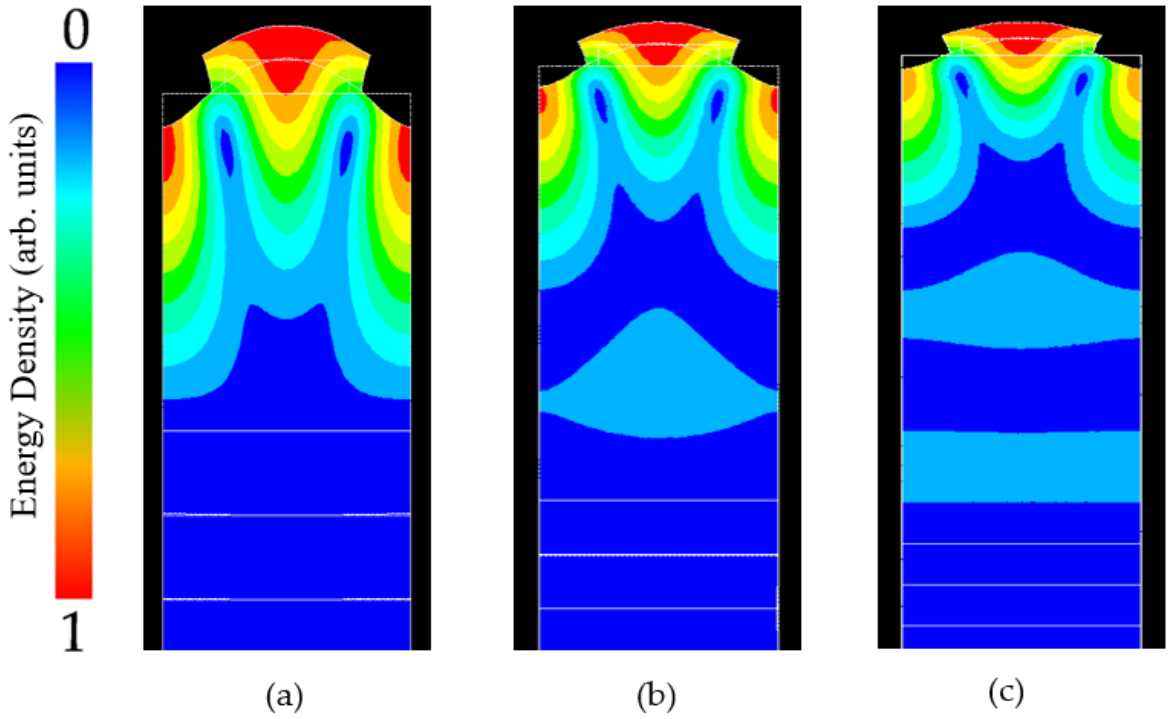


Figure 4.2: Kinetic energy density of the normal mode (at $\phi = 0$) corresponding to the SAW with different depths of silicon device layer: (a) $d = p$ (b) $d = 2p$ (c) $d = 3p$. Amplitude of kinetic energy density have been magnified.

wavelength silicon device layer will clearly distort the propagation of the SAW. Therefore, it is necessary to target the device layer thickness to be as close to the periodicity of the grating as possible. However, modest excursions (for example, 10-20 %) do not affect the performance dramatically.

Finally, the properties of thin films are typically different from that of bulk materials and depend on deposition techniques. Typically, it is only the Youngs modulus that has been measured to different. Both the Poisson's ratio and density are typically similar to bulk values for reasonable quality films. From the literature, the increase in Young's modulus in polycrystalline versus single crystal silicon is $\sim$ 30 % [31, 32], and the increase between thin

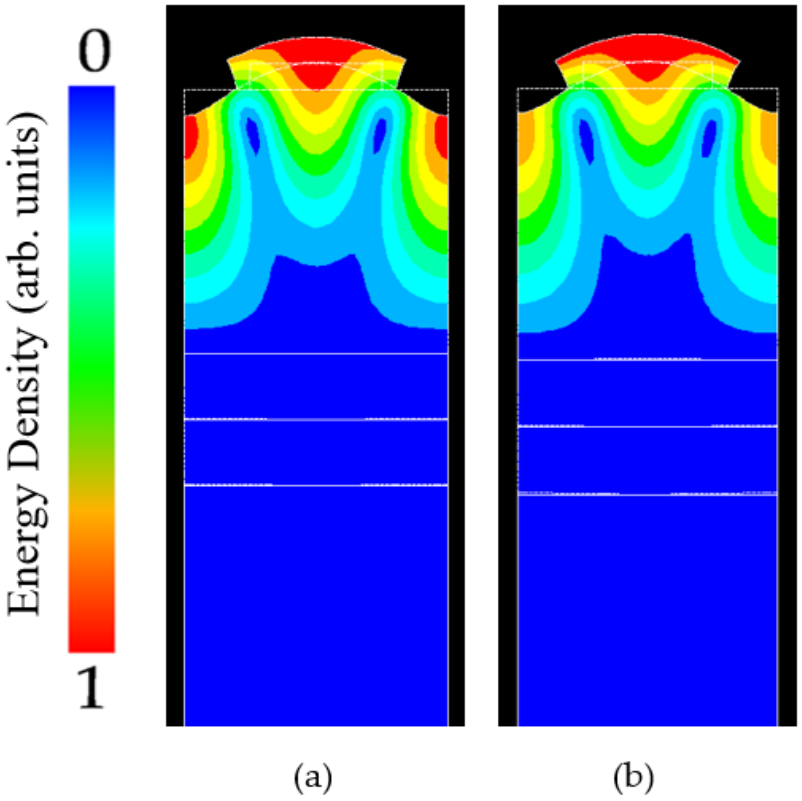


Figure 4.3: Kinetic energy density of the normal mode (at $\phi = 0$) corresponding to the SAW with (a) single crystal and (b) polycrystalline silicon device layer. Amplitude of kinetic energy density have been magnified.

film tungsten and bulk tungsten is $\sim$ 22 %[33, 34, 35]. The properties of thin film SiO_2 are in close agreement with their bulk values[36, 37]. Using simulations, we have confirmed that the confinement of energy is unaffected by such changes in film properties. Fig. 4.2 shows the kinetic energy density field of a SAW with single crystal and polycrystalline silicon device layer. However, a change in the properties of the top layer silicon does alter the frequency of the generated SAW, as expected. For example, there is an increase of 2 GHz between single crystal and polycrystalline silicon.

CHAPTER 5

SUMMARY AND CONCLUSIONS

In summary, we have investigated the damping of SAWs generated through optical excitation of a periodic metal grating. Various mechanisms such as bulk radiation, Akhiezer, thermoelastic and phonon-electron interactions serve to attenuate SAWs. At the lower (MHz) frequencies, the most dominant mechanism for attenuation is the interaction with thermal phonons with frequency dependence $\tau^{-1} \sim \omega^2$. In the GHz range, however, bulk radiation is several orders of magnitude more dissipative than any other mechanism due to a stronger frequency dependence, $\tau^{-1} \sim \omega^4$. Apart from metal and substrate properties, bulk radiation also depends on the duty cycle and is maximum at $\eta = 0.5$. We propose that the use of a one-layer acoustic Bragg reflector is sufficient to reduce damping due to bulk radiation. Our calculation show that the resulting damping time is larger than that due to the intrinsic damping time. We anticipate that the use of this structure will enable future measurements of the intrinsic damping times for SAWs at GHz frequencies. Such data can provide a good test of the various theories for intrinsic damping of SAWs at high frequencies.

REFERENCES

[1] A. R. Selfridge, "Approximate material properties in isotropic materials," *IEEE transactions on sonics and ultrasonics*, vol. 32, no. 3, pp. 381–394, 1985.

[2] J. Sadhu, J. Lee, and S. Sinha, "Frequency shift and attenuation of hypersonic surface acoustic phonons under metallic gratings," *Appl. Phys. Lett*, vol. 97, no. 13, p. 133106, 2010.

[3] D. P. Morgan, "A history of surface acoustic wave devices," *International journal of high speed electronics and systems*, vol. 10, no. 03, pp. 553–602, 2000.

[4] E. Salzmann, T. Plieninger, and K. Dransfeld, "Attenuation of elastic surface waves in quartz at frequencies of 316 mhz and 1047 mhz," *Applied Physics Letters*, vol. 13, no. 1, pp. 14–15, 1968.

[5] D. Nardi, M. Travagliati, M. E. Siemens, Q. Li, M. M. Murnane, H. C. Kapteyn, G. Ferrini, F. Parmigiani, and F. Banfi, "Probing thermomechanics at the nanoscale: impulsively excited pseudosurface acoustic waves in hypersonic phononic crystals," *Nano letters*, vol. 11, no. 10, pp. 4126–4133, 2011.

[6] Q. Li, K. Hoogeboom-Pot, D. Nardi, M. M. Murnane, H. C. Kapteyn, M. E. Siemens, E. H. Anderson, O. Hellwig, E. Dobisz, B. Gurney et al., "Generation and control of ultrashort-wavelength two-dimensional surface acoustic waves at nanoscale interfaces," *Physical Review B*, vol. 85, no. 19, p. 195431, 2012.

[7] H. Maris, "Attenuation of ultrasonic surface waves by phonon viscosity and heat conduction," *Physical Review*, vol. 188, no. 3, p. 1308, 1969.

[8] A. Maradudin and D. Mills, "Calculation of the anharmonic damping of rayleigh surface modes," *Physical Review*, vol. 173, no. 3, p. 881, 1968.

[9] A. Akheiser, *Journal of Physics, USSR*, p. 1277, 1939.

[10] A. Maznev, F. Hofmann, A. Jandl, K. Esfarjani, M. T. Bulsara, E. A. Fitzgerald, G. Chen, and K. A. Nelson, "Lifetime of sub-thz coherent acoustic phonons in a gaasalas superlattice," *Applied Physics Letters*, vol. 102, no. 4, p. 041901, 2013.

[11] J. Cuffe, O. Ristow, E. Chávez, A. Shchepetov, P.-O. Chapuis, F. Alzina, M. Hettich, M. Prunnila, J. Ahopelto, T. Dekorsy et al., "Lifetimes of confined acoustic phonons in ultrathin silicon membranes," *Physical review letters*, vol. 110, no. 9, p. 095503, 2013.

[12] R. Lifshitz and M. L. Roukes, "Thermoelastic damping in micro-and nanomechanical systems," *Physical review B*, vol. 61, no. 8, p. 5600, 2000.

[13] M. Lewis, "Attenuation of high-frequency elastic waves in quartz and fused silica," *The Journal of the Acoustical Society of America*, vol. 44, no. 3, pp. 713–716, 1968.

[14] W. P. Mason and H. E. Bömmel, "Ultrasonic attenuation at low temperatures for metals in the normal and superconducting states," *The Journal of the Acoustical Society of America*, vol. 28, no. 5, pp. 930–943, 1956.

[15] B. Daly, K. Kang, Y. Wang, and D. G. Cahill, "Picosecond ultrasonic measurements of attenuation of longitudinal acoustic phonons in silicon," *Physical Review B*, vol. 80, no. 17, p. 174112, 2009.

[16] S.-i. Tamura and T. Sakuma, "Theory of rayleigh-wave amplification in piezoelectric semiconductor filmsquantum theoretical approach," *Physical Review B*, vol. 15, no. 10, p. 4948, 1977.

[17] B. Bonello, A. Ajinou, V. Richard, P. Djemia, and S. Cherif, "Surface acoustic waves in the ghz range generated by periodically patterned metallic stripes illuminated by an ultrashort laser pulse," *The Journal of the Acoustical Society of America*, vol. 110, no. 4, pp. 1943–1949, 2001.

[18] M. E. Siemens, Q. Li, M. M. Murnane, H. C. Kapteyn, R. Yang, E. H. Anderson, and K. A. Nelson, "High-frequency surface acoustic wave propagation in nanostructures characterized by coherent extreme ultraviolet beams," *Applied Physics Letters*, vol. 94, no. 9, p. 093103, 2009.

[19] G. A. Antonelli, H. J. Maris, S. G. Malhotra, and J. M. Harper, "Picosecond ultrasonics study of the vibrational modes of a nanostructure," *Journal of applied physics*, vol. 91, no. 5, pp. 3261–3267, 2002.

[20] G. A. Antonelli, P. Zannitto, and H. J. Maris, "New method for the generation of surface acoustic waves of high frequency," *Physica B: Condensed Matter*, vol. 316, pp. 377–379, 2002.

[21] M. Bjornsson, A. Connolly, S. Mahat, B. Rachmilowitz, B. Daly, G. Antonelli, A. Myers, K. Singh, H. Yoo, and S. King, "Picosecond ultrasonic study of surface acoustic waves on titanium nitride nanostructures," *Journal of Applied Physics*, vol. 117, no. 9, p. 095305, 2015.

[22] D. Nardi, F. Banfi, C. Giannetti, B. Revaz, G. Ferrini, and F. Parmigiani, "Pseudosurface acoustic waves in hypersonic surface phononic crystals," *Physical Review B*, vol. 80, no. 10, p. 104119, 2009.

[23] H. J. Maris, "Interaction of sound waves with thermal phonons in dielectric crystals," *Physical Acoustics*, vol. 8, pp. 279–345, 2012.

[24] L. Landau and G. Rumer, "Absorption of sound in solids," *Phys. Z. Sowjetunion*, vol. 11, no. 18, 1937.

[25] A. Pippard, "Cxxii. ultrasonic attenuation in metals," *The London, Edinburgh, and Dublin Philosophical Magazine and Journal of Science*, vol. 46, no. 381, pp. 1104–1114, 1955.

[26] H.-N. Lin, H. Maris, L. Freund, K. Lee, H. Luhn, and D. Kern, "Study of vibrational modes of gold nanostructures by picosecond ultrasonics," *Journal of applied physics*, vol. 73, no. 1, pp. 37–45, 1993.

[27] A. Maradudin and D. Mills, "Attenuation of rayleigh surface waves by surface roughness," *Applied Physics Letters*, vol. 28, no. 10, pp. 573–575, 1976.

[28] S. M. Goodnick, D. K. Ferry, C. Wilmsen, Z. Liliental, D. Fathy, and O. Krivanek, "Surface roughness at the si (100)-sio 2 interface," *Physical Review B*, vol. 32, no. 12, p. 8171, 1985.

[29] W. Wang and D. Weinstein, "Acoustic bragg reflectors for q-enhancement of unreleased mems resonators," in *Frequency Control and the European Frequency and Time Forum (FCS), 2011 Joint Conference of the IEEE International*. IEEE, 2011, pp. 1–6.

[30] A. M. APDL, "Mechanical applications theory reference," *ANSYS Release*, vol. 13, 2010.

[31] D. Maier-Schneider, A. Köprülülü, S. B. Holm, and E. Obermeier, "Elastic properties and microstructure of lpcvd polysilicon films," *Journal of Micromechanics and Microengineering*, vol. 6, no. 4, p. 436, 1996.

[32] W. N. Sharpe Jr, B. Yuan, R. Vaidyanathan, and R. L. Edwards, "New test structures and techniques for measurement of mechanical properties of mems materials," in *Micromachining and Microfabrication'96*. International Society for Optics and Photonics, 1996, pp. 78–91.

[33] R. Saha and W. D. Nix, "Effects of the substrate on the determination of thin film mechanical properties by nanoindentation," *Acta Materialia*, vol. 50, no. 1, pp. 23–38, 2002.

[34] C.-E. Morosanu and V. Soltuz, "Kinetics and properties of chemically vapour-deposited tungsten films on silicon substrates," *Thin Solid Films*, vol. 52, no. 2, pp. 181–194, 1978.

[35] P.-O. Renault, K. Badawi, L. Bimbault, P. Goudeau, E. Elkaım, and J. Lauriat, "Poissons ratio measurement in tungsten thin films combining an x-ray diffractometer with in situ tensile tester," *Applied physics letters*, vol. 73, no. 14, pp. 1952–1954, 1998.

[36] J.-H. Zhao, T. Ryan, P. S. Ho, A. J. McKerrow, and W.-Y. Shih, "Measurement of elastic modulus, poisson ratio, and coefficient of thermal expansion of on-wafer submicron films," *Journal of applied physics*, vol. 85, no. 9, pp. 6421–6424, 1999.

[37] G. Carlotti, L. Doucet, and M. Dupeux, "Comparative study of the elastic properties of silicate glass films grown by plasma enhanced chemical vapor deposition," *Journal of Vacuum Science & Technology B*, vol. 14, no. 6, pp. 3460–3464, 1996.